minerals

MDPI

Article

KOH-Based Hydrothermal Synthesis of Iron-Rich Titanate Nanosheets Assembled into 3D Hierarchical Architectures from Natural Ilmenite Mineral Sands

Karina J. Lagos [1,2], Bojan A. Marinkovic [3,*], Anja Dosen [4], Alexis Debut [5], Karla Vizuete [5], Victor H. Guerrero [2], Emilio Pardo [1] and Patricia I. Pontón [2,*]

[1] Molecular Science Institute, Coordination Chemistry Group, University of Valencia, 46980 Paterna, Spain; karina.lagos@epn.edu.ec (K.J.L.); emilio.pardo@uv.es (E.P.)
[2] Department of Materials, Escuela Politécnica Nacional (EPN), Quito 170525, Ecuador
[3] Department of Chemical and Materials Engineering, Pontifical Catholic University of Rio de Janeiro (PUC-Rio), Rio de Janeiro 22453-900, Brazil
[4] International Centre for Diffraction Data (ICDD), Newtown Square, PA 19073, USA; dosen@icdd.com
[5] Centro de Nanociencia y Nanotecnología, Universidad de las Fuerzas Armadas (ESPE), Sangolquí 171103, Ecuador; apdebut@espe.edu.ec (A.D.); ksvizuete@espe.edu.ec (K.V.)
* Correspondence: bojan@puc-rio.br (B.A.M.); patricia.ponton@epn.edu.ec (P.I.P.)

Abstract: The synthesis of titanate nanostructures from low-cost mineral precursors is a topic of continuous interest, considering not only their fundamental aspects but also the benefits of incorporating such nanomaterials in a wide variety of applications. In this work, iron-rich titanate nanosheets were synthesized from Ecuadorian ilmenite sands (ilmenite–hematite solid solution-IHSS) through an alkaline hydrothermal treatment (AHT) using potassium hydroxide (KOH). The effect of the duration of the KOH-AHT was assessed at 180 °C for 24, 48, 72, and 96 h. The morphology evolution over time and the plausible formation mechanisms of titanate nanostructures were discussed. The most significant morphological transformation was observed after 72 h. At this time interval, the titanate nanostructures were assembled into well-defined 3D hierarchical architectures such as book-block-like arrangements with open channels. Based on X-ray powder diffraction (XRPD), transmission electron microscopy (TEM), selected area electron diffraction (SAED), and scanning electron microscopy coupled with energy-dispersive X-ray spectroscopy (SEM-EDS) analyses, it was determined that these nanostructures correspond to iron-rich layered titanates (Fe/Ti mass ratio of 7.1). Moreover, it was evidenced that the conversion of the precursor into layered nanostructures was not complete, since for all the tested reaction times the presence of remaining IHSS was identified. Our experiments demonstrated that the Ecuadorian ilmenite sands are relatively stable in KOH medium.

Keywords: titanate-based nanosheets; black sands; ilmenite sand dissolution; potassium titanates

Citation: Lagos, K.J.; Marinkovic, B.A.; Dosen, A.; Debut, A.; Vizuete, K.; Guerrero, V.H.; Pardo, E.; Pontón, P.I. KOH-Based Hydrothermal Synthesis of Iron-Rich Titanate Nanosheets Assembled into 3D Hierarchical Architectures from Natural Ilmenite Mineral Sands. *Minerals* **2023**, *13*, 406. https://doi.org/10.3390/min13030406

Academic Editors: Qinghua Zeng, Hao Ding and Xuefeng Dong

Received: 14 February 2023
Revised: 9 March 2023
Accepted: 14 March 2023
Published: 15 March 2023

1. Introduction

Alkaline hydrothermal treatment (AHT) has been widely applied for the synthesis of a diversity of titanate-based nanostructures due to its simplicity and low energy consumption [1]. Kasuga et al. proposed for the first time in 1998 the synthesis of titanate nanotubes from a commercial synthetic TiO_2 precursor through AHT using a concentrated NaOH solution [2]. Since then, several researchers have confirmed, in a short time span, the effectiveness of this route [3–5]. The AHT conditions can determine a variety of distinct morphologies of titanate nanostructures, with the general chemical formula of $A_2Ti_nO_{2n+1}$ (A = alkali metal ion or proton, n = 3–6). These nanostructures include nanoparticles, nanosheets, nanotubes, nanoribbons, nanowires, nanorods, and nanofibers [6–9]. Thus, different temperatures, reaction times, concentrations, types of alkaline solutions, and precursors have been assessed. From the point of view of materials design, the AHT represents

a very attractive, versatile, and rapid route to tailor -morphology, composition, and other properties of titanate nanostructures. The selected parameters will depend on the nature of the precursor, the equipment available, and above all, the desired characteristics of the synthesized titanates.

In this context, a more affordable alternative to produce titanate-based nanostructures has emerged, consisting of the use of low-cost precursors. Mineral sands, based on rutile or ilmenite [10–14], have been suggested as substitutes for the conventional synthetic TiO_2 precursors (anatase, rutile or their mixture). For instance, iron-doped titanate-based nanostructures, the so-called ferrititanates, have been attained as the main phase after processing Brazilian ilmenite sands with AHT using NaOH concentrate solutions [12,13,15,16]. Ilmenite and rutile were the main components of this precursor, and pseudorutile and quartz were identified as secondary phases. The Fe/Ti mass ratio of this mineral precursor of ~0.8 was considered titanium-rich sand [12]. Thus, lepidocrocite-like ferrititanate nanosheets along with small amounts of hematite nanoparticles have been synthesized using AHT (at 130 °C for 70 h with 10 M NaOH) [12,13,15]. Ferrititanate submicron and micron crystals with a $CaFe_2O_4$ structure type group, along with magnetite, have also been obtained (applying 190 °C for 70 h with 10 M NaOH) [16]. The presence of iron in the synthesized products comes from the natural elemental composition of the precursor (ilmenite sands). It is evident that iron not only can be part of the titanate structure, but also can reprecipitate as iron oxide nanoparticles such as hematite or magnetite.

In light of this, in our previous work, we demonstrated the feasibility to employ Ecuadorian ilmenite mineral sands as a low-cost precursor to prepare nanostructures through AHT (at 180 °C for 72 h with 10 M NaOH) [17]. The following titanate nanostructures were obtained: (i) nanobelts possibly belonging to iron-doped sodium hexatitanate structures, and (ii) nanoparticle agglomerates (performing a precursor pretreatment) probably corresponding to corrugated sodium iron-rich trititanates [17]. As the authors are aware, this is the only work that has reported the harnessing of Ecuadorian ilmenite sands to synthesize titanate-based nanostructures so far. It is important to point out that the Ecuadorian sands have a different chemical and phase composition compared to the Brazilian ones, viz., ilmenite–hematite solid solution (IHSS), with traces of zircon and orthoclase. Their Fe/Ti mass ratio is 2.8, being classified as an iron-rich precursor. Considering these different features of Ecuadorian ilmenite sands precursor, only a partial conversion into the aforementioned titanate nanostructures was accomplished [17]. These results paved the way for the preparation, in just one step, of hybrid materials with specific morphologies and potential applications. Thus, there is still plenty of room to explore AHT using Ecuadorian ilmenite mineral sands as a low-cost precursor (~USD 24 is the price per MT).

The development of iron-rich titanate nanostructures has been continuously studied [18–20]. The presence of iron brings modifications to the titanate-based structures, causing an improvement to the optical and photocatalytic properties [21]. It has been demonstrated that the incorporation of iron in the crystal structure reduces the band gap [13,22]. This effect promotes a shift in the absorption spectra toward higher wavelengths, enhancing the efficiency of the light absorption, encompassing not only the ultraviolet region, but also the visible range, which is not absorbed in iron-free titanates [13,22]. Iron doping can also induce magnetism in ferroelectric titanates, such as $BaTiO_3$ [23], or higher electrochemical capacity in compounds such as $Li_4Ti_5O_{12}$ [24]. Regarding the potential applications of ferrititanates, their use as catalysts and ion exchangers has been reported in the literature, commonly within the fields of water remediation [25,26].

Moreover, this type of material, composed of layered nanostructures, becomes a good candidate as a filler in the preparation of polymer composites. Its integration into polymer matrices can improve their mechanical and/or gas barrier properties [15,27], especially when they exhibit the morphology of nanotubes and nanosheets due to the high degree of interfacial interaction between the nanofiller and the polymer matrix [28,29].

Likewise, owing to the high stability and sensitivity of iron oxide-based materials, such as hematite, they have been successfully employed as sensors of a number of vapors

or gases such as ethanol [30], oxygen [31], hydrogen [32], hydrogen sulfide [33], and liquefied petroleum gas [34], among others. In fact, it has been proved that the morphology influenced the charge transfer resistance, gas sensitivity, response time, and recovery time [34].

Regarding the preparation of titanate nanostructures using AHT, several authors have confirmed that one of the most important parameters to tailor and control the characteristics of these nanomaterials, apart from the temperature, is the type of alkaline solution [35–37]. Having this in mind, herein we propose the usage of a concentrated solution of potassium hydroxide (KOH 10 M) to study the changes that Ecuadorian ilmenite mineral sands undergo when a distinct alkaline media is employed in the AHT. The temperature chosen for the treatment was 180 °C, and we assessed the effect of KOH-AHT exposure time (24, 48, 72, and 96 h) on the morphology, chemical and phase composition of the as-synthesized powders (KOH-AHT products). The KOH-AHT products were characterized using SEM-EDS, TEM, SAED and XRPD.

2. Materials and Methods

2.1. KOH-AHT Procedure

AHTs were performed using milled Ecuadorian ilmenite sands [38] as the precursor. The grinding procedure was previously described by Lagos et al. [17]. Briefly, the sands were milled at 300 rpm for 9 min using a planetary mill with a ball to sand mass ratio of 20.

Defined amounts of the precursor (1.75 g) and KOH 10 M solution (350 mL) were added into a reactor (Berghof BR-500, Baden-Württemberg, Germany). The syntheses were carried out at the maximum allowable temperature of the equipment (180 °C) under constant stirring (350 rpm) for different reaction times of 24, 48, 72, and 96 h. Afterward, the system was cooled to room temperature and the KOH-AHT products were recovered using decantation, followed by filtration. The KOH-AHT products were washed with distilled water until reaching neutral pH. Finally, the samples were dried in a stove at 80 °C for 12 h, and ground manually in an agate mortar. An illustration of the as-mentioned procedure is depicted in Figure 1.

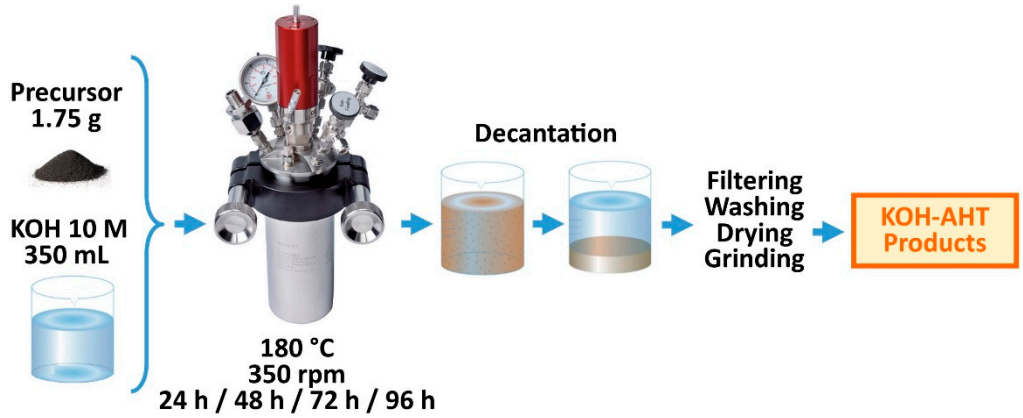

Figure 1. Procedure for preparation of KOH-AHT-products.

It is important to note that additional experiments were carried out, trying to improve the dissolution of the precursor. Even though these experiments will not be discussed in this work, it is worth mentioning that different AHT conditions were examined. The three most relevant were (i) a higher KOH concentration (12 M), (ii) an elevated pressure (~30 bar, reached with the addition of N_2), and (iii) consecutive AHTs (with a total KOH-AHT exposure time of 144 h). Nevertheless, in none of the above conditions the Ecuadorian sands were completely dissolved in KOH medium, since remaining precursor particles were identified after the treatments (see Figure S1 in the Supplementary Material). Furthermore, the obtained KOH-AHT products did not present the formation of 2D nanostructured morphologies. Therefore, we selected to discuss the effect of the AHT conditions described

firstly, since this procedure resulted in the most significant change in the morphology of the milled Ecuadorian ilmenite mineral sands.

2.2. Characterization of KOH-AHT Products

The analyses of the morphology and particle size of the precursor and the as-synthesized KOH-AHT products were performed with SEM (Tescan Mira 3, South Moravian, Czech Republic) operating at 10 kV. The elemental composition of each KOH-AHT product was determined using EDS at 25 kV accelerating voltage. The SEM analyses were performed without deposition of a conduction layer. The KOH-AHT product obtained at 72 h was additionally characterized using TEM at 80 kV (FEI Tecnai G2 Spirit Twin, North Brabant, The Netherlands) to obtain images and SAED patterns. The latter was analyzed using CrysTBox software [39].

XRPD measurements were conducted using Cu Kα radiation (Bruker D2 Advance, Karlsruhe, Germany) in the 2θ range of 5° to 60° in 0.02° steps and a count time of 0.6 s per step with rotation (sample spinner). Power Diffraction File ^{TM} [40] PDF 2 database was used to identify the crystalline phases. The pattern fitting was performed in Jade MDI.

3. Results

3.1. SEM and TEM Analyses

Figure 2 shows the morphology of the precursor, composed of irregular particles, with sizes ranging from hundreds of nanometers to a few tens of micrometers. These features are typical for a powder after a dry milling procedure.

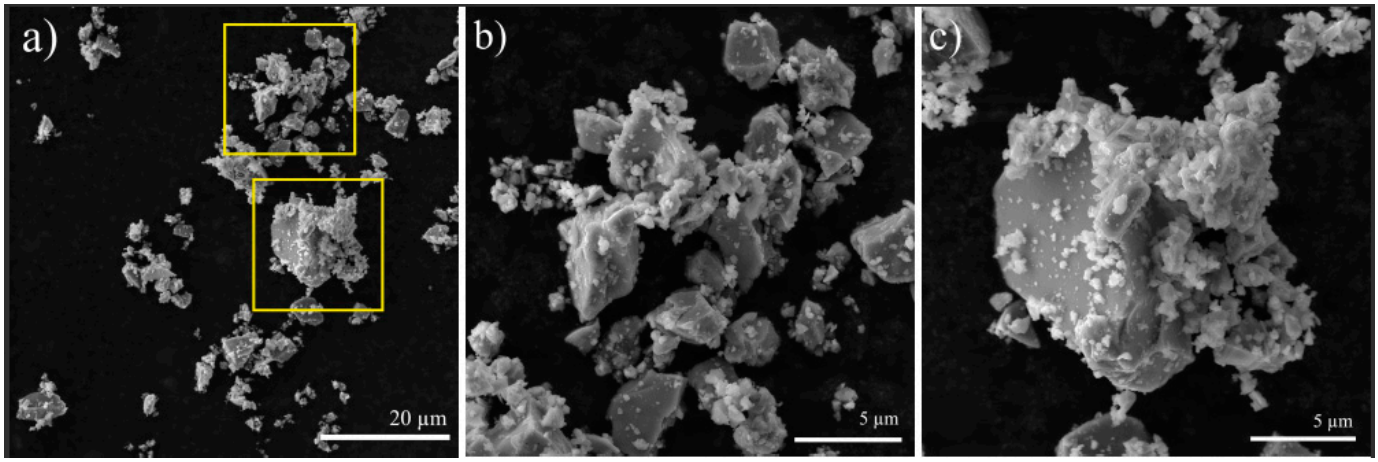

Figure 2. (**a**–**c**) SEM images of the powder precursor (milled Ecuadorian ilmenite sands).

The morphology evolution of the Ecuadorian ilmenite mineral sands subjected to KOH-AHT at 180 °C for 24, 48, 72, and 96 h is presented in Figure 3. After 24 h of reaction time, a change in morphology begins to be noticed, since scarce nanosheets started to appear assembled in the form of a house-of-cards architecture (see Figure 3a,b). An SEM image at higher magnification of these nanosheets is presented in Figure 4a.

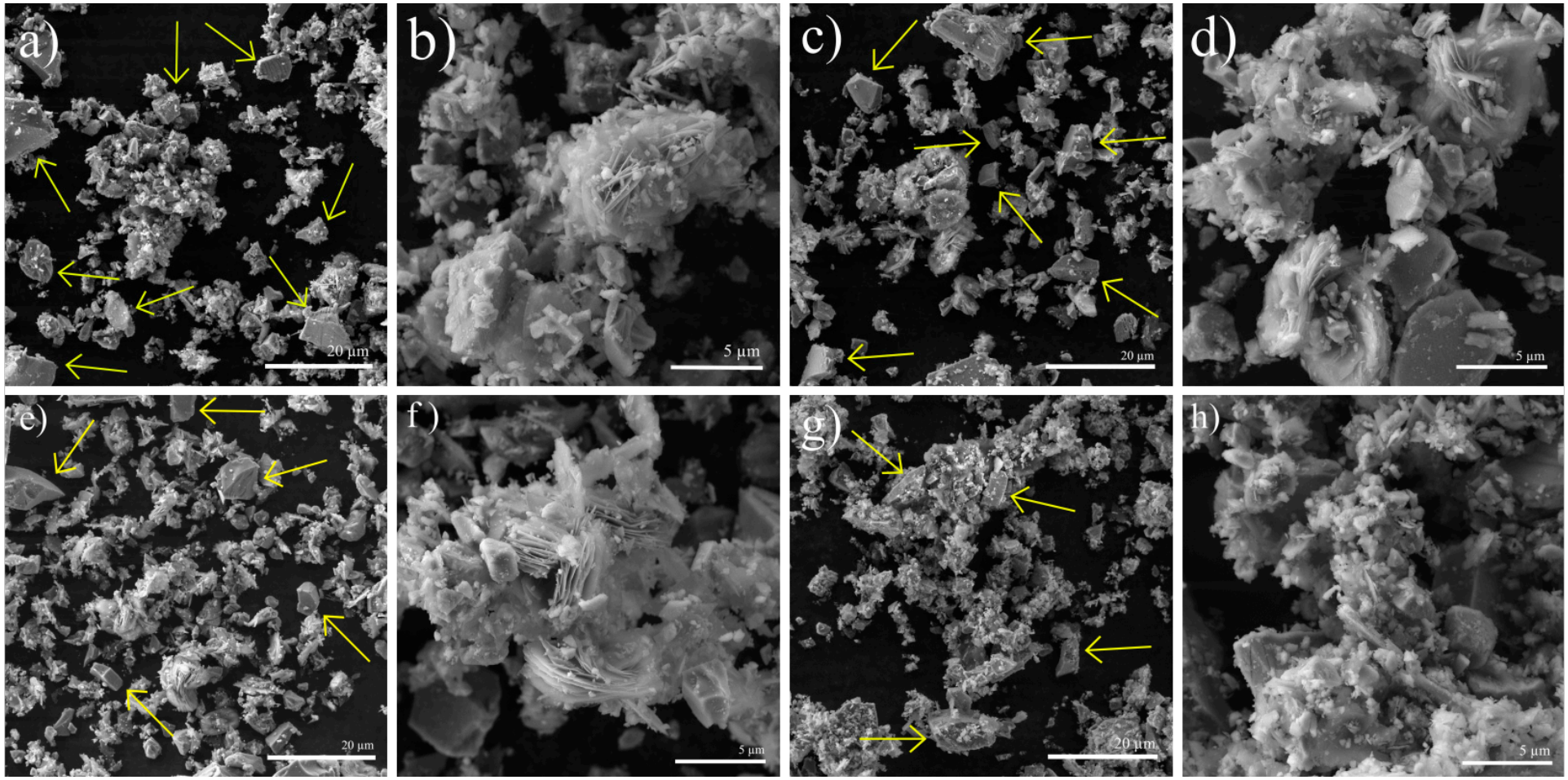

Figure 3. SEM images of KOH-AHT products obtained at (**a**,**b**) 24 h, (**c**,**d**) 48 h, (**e**,**f**) 72 h, and (**g**,**h**) 96 h.

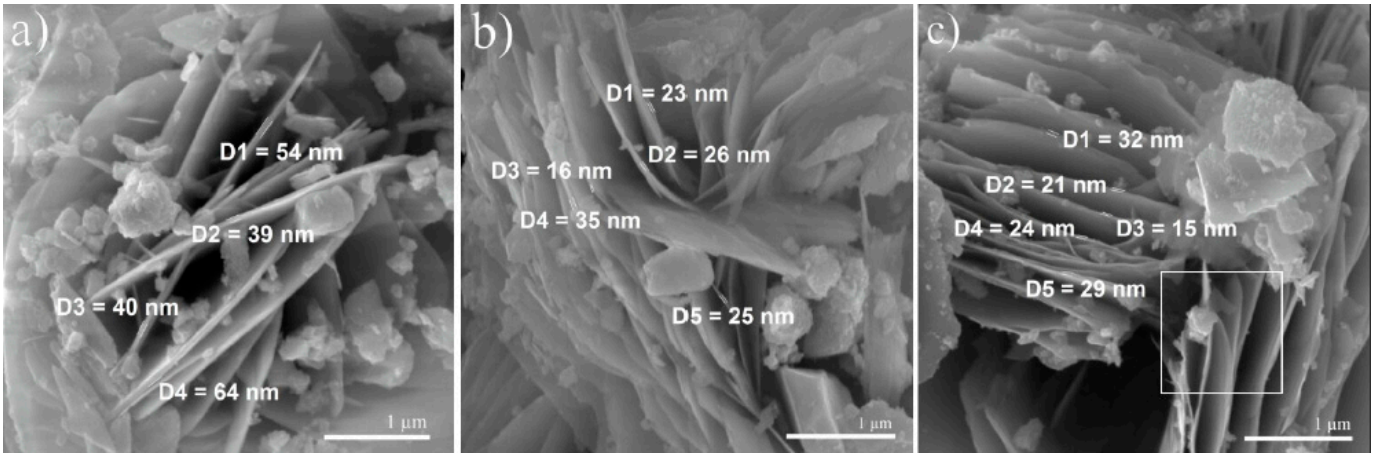

Figure 4. SEM images of nanosheets obtained at (**a**) 24 h, (**b**) 48 h, and (**c**) 72 h.

The KOH-AHT product obtained at 48 h exhibited nanosheets similar to those described for the process at 24 h (see Figure 3c,d). The main difference lies in the fact that their number seems to be slightly superior to that observed at 24 h (see Figure 3d).

At 72 h of reaction, several nanosheets were identified and the most significant transformation in morphology was observed (see Figure 3e). The self-organized hierarchical assemblies had the appearance of a 3D lamellar architecture composed of nanosheets separated by open channels. The thicknesses of the nanosheets were in the range of 15 to 32 nm, which in turn were constituted from many stacked 2D ultrathin layers (see the square in Figure 4c).

Regarding the KOH-AHT product obtained at 96 h, the SEM images presented in Figure 3g,h show that the morphology was not well-defined and it seems that there was no notable presence of nanosheets.

It is worth noting that remaining precursor particles were observed in all the KOH-AHT products (marked with arrows in Figure 3a,c,e,g).

The KOH-AHT product obtained at 72 h was also identified using TEM as nanosheets (see Figure 5a,b). These results were consistent with the SEM characterization. The length of these nanosheets was within the submicron and micron scale. Figure 5c shows the indexed SAED pattern of the phase with nanosheet morphology (formed in the KOH-AHT), indicating that this presents a $K_2Ti_4O_9$-like structure. This was determined through simulation of SAED (by using CIF file PDF Card 00-032-0861). Moreover, the spots observed in Figure 5c demonstrated that the nanosheets were crystalline.

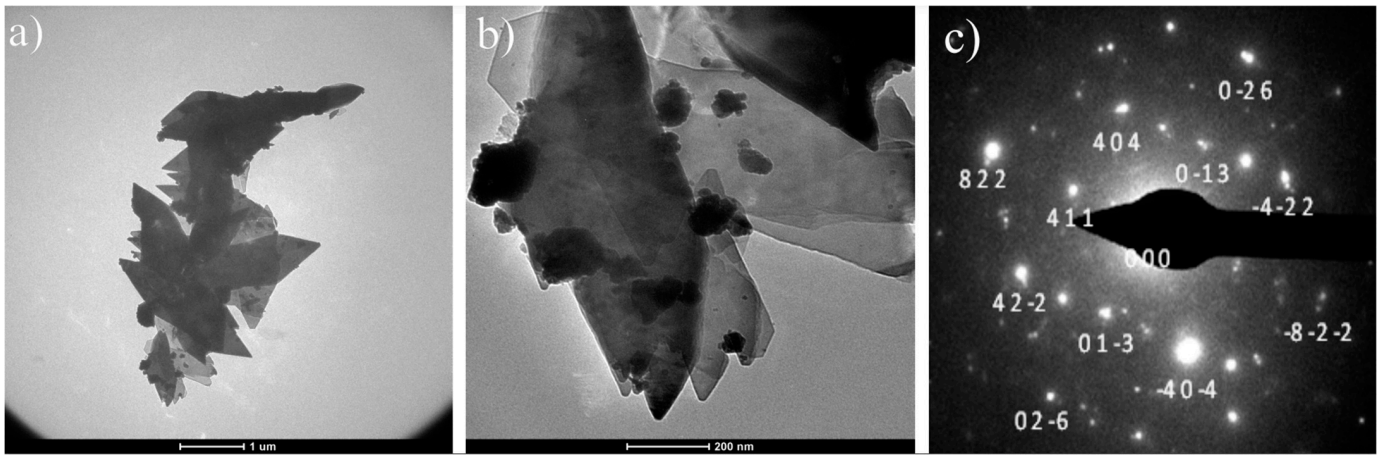

Figure 5. (**a**,**b**) TEM images of KOH-AHT product obtained after 72 h showing the nanosheets morphology, (**c**) the corresponding SAED pattern.

Additionally, SEM-EDS semiquantitative elemental analyses were carried out for the precursor and for the nanosheets synthesized after 24, 48, and 72 h. The results are presented in Table 1.

Table 1. EDS semiquantitative elemental analyses * of the precursor and nanosheets obtained at different KOH-AHT times.

Sample	Morphology	Fe Content (wt. %)	Ti Content (wt. %)	K Content (wt. %)	Fe/Ti Mass Ratio
Precursor	Irregular particles	75.40 ± 1.51	24.60 ± 0.55	-	~3.1
24 h	Nanosheets	73.51 ± 1.29	23.21 ± 1.24	3.28 ± 0.24	~3.2
48 h	Nanosheets	81.54 ± 0.63	17.01 ± 0.43	1.44 ± 0.10	~4.8
72 h	Nanosheets	87.06 ± 3.69	12.18 ± 0.49	0.75 ± 0.04	~7.1

* These values exclude the oxygen weight percentage.

3.2. XRPD Analyses

The XRPD patterns of all the KOH-AHT products and the precursor (milled Ecuadorian ilmenite sands) are depicted in Figure 6. Regarding the precursor, it corresponded to an IHSS ($0.6(FeTiO_3)0.4(Fe_2O_3)$, PDF 04–017–0669, called IHSS1) rich in ilmenite phase, as revealed by the Le Bail qualitative method [17,38]. Nevertheless, when the quantitative analysis was performed in Jade MDI (see Figure S2 in the Supplementary Material), the XRPD pattern for the precursor was better fitted when an additional IHSS ($0.8(FeTiO_3)0.2(Fe_2O_3)$, PDF 01–070–6223, called IHSS2) richer in ilmenite was considered. This IHSS2 comprises a minor phase representing approximately a third part of the major phase (IHSS1).

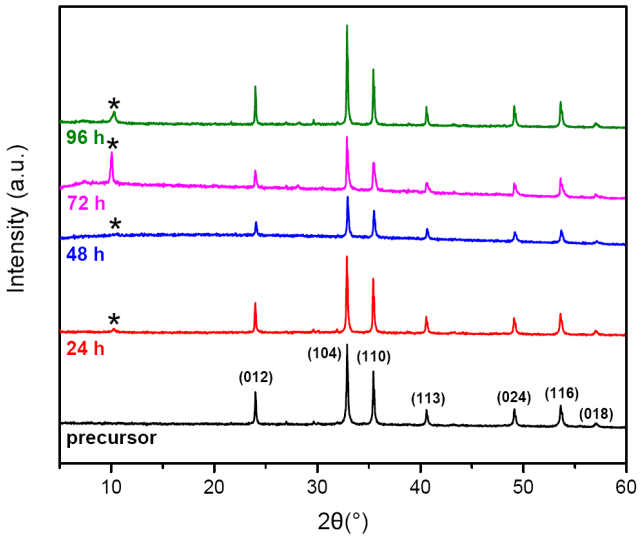

Figure 6. XRPD patterns of the precursor and the KOH-AHT products obtained at 24, 48, 72, and 96 h. * Stands for the layered titanate.

Note that the characteristic peaks ascribed to the precursor also appeared in the XRPD patterns of all the KOH-AHT products (see Figure 6), corroborating that the KOH-AHT exposure promoted only a partial conversion of the precursor. This was consistent with SEM images presented in Figure 3 showing remaining ilmenite sand particles. Based on the XRPD results, it is important to indicate that the presence of IHSS2 was not detected within the KOH-AHT products, suggesting that this phase was completely dissolved from the first reaction time (24 h).

In the KOH-AHT products (24, 48, 72, and 96 h) a typical diffraction line of layered titanates appeared at ~10° (marked as *), corresponding to the (200) basal reflection [12,13,27]. The intensity of this peak was highest at 72 h; however, this should not be used as an indication of the quantity of layered titanates inside the samples, since it also could be a consequence of the preferential orientation effect, common for layered phases.

4. Discussion

The SEM images presented in Figure 3 evidenced the morphology changes that occurred when Ecuadorian ilmenite mineral sands were subjected to an AHT with a KOH solution (10 M) at 180 °C at different time intervals. It was determined that the morphology and structure of the KOH-AHT products were time dependent. Additionally, as the KOH-AHT time increased, it appears that the precursor was more consumed and the number of large unreacted particles decreased (see Figure 3a,c,e,f). This was probably due to the solubility of the precursor, which is generally sensitive to the particle size. Thus, the smallest particles were more susceptible to dissolution owing to higher contributions of the excess surface Gibbs free energy [41], while the larger ones might only show surface dissolution. This can be observed, for instance, in some of the larger particles of the remaining precursor within the KOH-AHT product obtained at 24 h. In this case, etching was identified, triggering a rougher and more flawed surface compared to that of the untreated precursor (see Figure S3 in the Supplementary Material) [41].

Regarding the XRPD patterns of the KOH-AHT products, the intensity of the peak at 10° 2θ increased up to 72 h, which can be attributed to the presence of layered titanates (see Figure 6). The ratios between the intensity of the main peak of the precursor (~33° 2θ) and that of the titanate phase (~10° 2θ) were 18.5, 13.5, 1.7, and 9.7 for the 24, 48, 72, and 96 h treatments, respectively. Nonetheless, it should be considered that the intensity of the peak at 10° 2θ was not only related to the intrinsic features, such as the amount of transformation of the precursor into titanates, but also to the preferential orientation effect. Thus, the lowest ratio of 1.7 (at 72 h) could have been a consequence of the better stacking of the nanosheets as a book-block-like structure.

Due to the lack of more diffraction lines of the titanate phase (only one at ~10° 2θ can be ascribed to this phase), its identification was not possible using XRPD analysis. Nevertheless, in accordance with the TEM-SAED analysis, the titanate phase was tentatively assigned to a lamellar potassium titanate with a $K_2Ti_4O_9$-like structure (PDF 00–032–0861) [42]. It should be noted that this $K_2Ti_4O_9$ exhibits a notable ion exchange capacity [43,44]. It is also probable that this phase suffered some intercalation of hydrogen due to the washing process of the KOH-AHT products with distilled water, becoming $K_{2-x}H_xTi_4O_9$. Therefore, $K_{2-x}H_xTi_4O_9$ stoichiometry might be suggested for the nanosheets [45,46], where x depends on the ion exchange ($K^+ \leftrightarrow H^+$). This may explain the low content of potassium (see Table 1).

Likewise, it is important to highlight that the nanosheets had a high content of iron in their composition. This indicates that the $K_{2-x}H_xTi_4O_9$ phase was greatly enriched with iron, which probably substituted partially for titanium. In fact, the nanosheets presented an increment in iron over time, since the values of the Fe/Ti mass ratio increased from 3.2 to 7.1 at 24 and 72 h, respectively (see Table 1). Keeping in mind that the ilmenite precursor is composed of a 50.4 wt. % of iron and 18.6 wt. % of titanium, it is most likely that the reaction medium was enriched in iron, explaining its high content in the nanosheets. In addition, it has been proven that depending on the degree of iron doping, the cation exchange capacity of the titanate nanostructures can be improved [47,48]. Thus, this could be the reason why the potassium content decreased within the nanosheets over time (see Table 1).

Regarding the formation mechanism of the titanate nanostructures obtained with AHT, it is still quite controversial [49,50]. However, based on our results and also those from related works reported in literature [8,37,51–53], we supported a model for the formation of iron-rich titanate nanosheets assembled in 3D hierarchical architectures (see Figure 7).

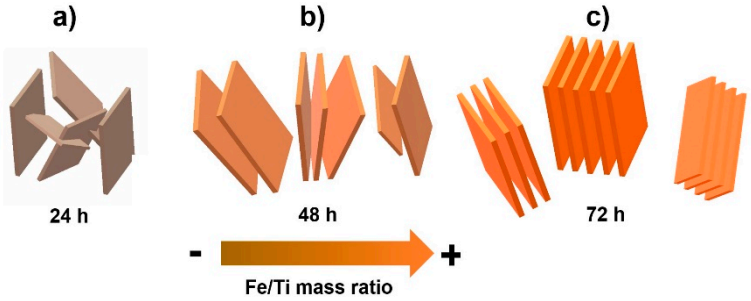

Figure 7. Scheme of the proposed formation mechanism of the nanosheets assembled into 3D hierarchical architectures: (**a**) few nanosheets appeared as house-of-cards arrangements, (**b**) the quantity of nanosheets seems higher and better stacked, (**c**) the well-organized assembly presented a book-block-like appearance with open channels.

In the first stage, the precursor (ilmenite mineral sands) starts to dissolve. As the duration of KOH-AHT exposure increases, the consumption (dissolution) of the precursor also increases. Hence, during dissolution, TiO_6 octahedra, monotitanate, or polytitanic species might be generated. At the same time, K^+ ions from the alkaline solution were available, reacting with the titanium species, nucleating titanate nanosheets [8,51], composed by a few ultrathin layers with K^+ acting as compensation charge interlayer cations. As stated before, during the dissolution of the precursor, iron species were also set free. Therefore, the reaction medium had a considerable amount of dissolved iron, which substituted titanium partially in octahedra sites of the titanate-layered nanostructures. This affirmation is based on the homogeneous distribution of iron in the as-prepared nanosheets, determined using elemental mapping of the KOH-AHT product obtained at 72 h (see the Supplementary Material Figure S4).

After 24 h of reaction time, morphological changes started to be noticed. The initial nanosheets presented a house-of-cards configuration (see Figures 3b and 4a). As the dissolution proceeded, more reactive titanium and iron species would be expected to be released. Consequently, the number of titanate nanosheets might increase over time (see Figures 3d and 4b). In addition, the stacking of the nanosheets also improved, giving rise to well-organized stacked 3D architectures with the appearance of a book-block-like structure in which the pages (nanosheets) were separated by open channels (see Figures 3f and 4c). It is likely that this stacking process to form better organized architectures was promoted by the electrostatic attraction between adjacent nanosheets [37], resulting in a surface area reduction as a mechanism to decrease the nanosheets' surface energy [52]. Moreover, the nanosheets were quite planar without exhibiting noticeable curvature. This suggests that their surface had a balanced charge of H^+ and K^+ due to a symmetric chemical environment [53]. Similar morphologies of 3D architectures of well-stacked In_2O_3 nanosheets with open channels, prepared using a hydrothermal method, have been reported in the literature [52].

Furthermore, comparable nanosheets, although not assembled in 3D hierarchical architectures, were reported by Costa et al. [13] and Jardim et al. [12]. They prepared iron-rich nanosheets, that were ascribed to a lepidocrocite-like structure, using NaOH-AHT (10 M at 110–150 °C) with an ilmenite titanium-rich precursor (~33 wt. % of titanium and ~27 wt. % of iron). They also obtained a homogeneous elemental distribution of iron in the nanosheets due to iron-doping. However, the iron-doped titanate nanosheets synthesized by these authors were thinner, with thicknesses of approximately 10 nm, comprising around 20 ultrathin layers [12]. The thicknesses of the nanosheets within the KOH-AHT product obtained at 72 h were in the range of 15 to 32 nm (see Figure 4c), as aforementioned. This thickening may have been a result of an enhanced capture of dissolved titanates and iron species from the KOH alkaline media into the nanosheets [54].

Regarding the morphology of the product obtained at the longer KOH-AHT exposure of 96 h, it showed irregular shaped micro and nanostructures. Note that solely scarce

nanosheets were detected (see Supplementary Material Figure S5), since no well-defined morphologies were identified (see Figure 3g–h). It can be proposed that the plausible dissolution of the nanosheets could be a consequence of the prolonged AHT [55].

In our previous work, we carried out a similar AHT using the same synthesis conditions employed in this work at 72 h. The difference resided in the type of alkaline medium, sodium hydroxide (NaOH 10 M) was used in the previous study [17]. Thus, it was evident that this variation significantly impacted the morphology, chemical and phase composition of the synthesized titanates. Through NaOH-AHT, the synthetized titanate nanostructures corresponded to bundles of nanobelts, while with KOH-AHT, nanosheets assembled into 3D arrangements were obtained. Hence, even using the same concentration of the alkaline solution and equal synthesis temperature, it is clear that the type of alkaline medium promotes drastic modifications in titanate morphology. In fact, the mechanism of formation is apparently different.

In the case of titanate nanobelts obtained through NaOH-AHT, they might be formed by an orderly sticking of previously formed intermediate nanosheets and their coalescence and splitting into nanobelts (nanofibers or nanowires) at a later stage [51,54]. It should be noted that when using commercial synthetic TiO_2 precursors within NaOH-AHTs, there is an established morphology evolution which comprises nanosheets, nanotubes, and finally, nanofibers (nanowires) [56]. These three successive unavoidable nanostructures appear by an increment in either the concentration of the alkaline solution or the temperature. However, when using ilmenite sands as precursors within NaOH-AHTs, the sequence of the morphology evolution of the titanates apparently differs. Until now, the formation of titanate nanotubes from ilmenite mineral sands precursors has not been reported; thus, the formation mechanism could involve nanosheets at first and nanofibers (nanobelts or nanowires) in the later stages [13,17].

The differences between the morphology of the products synthetized from KOH-AHT and NaOH-AHT could be a consequence of the difference in the solubility of the precursor. It has been proven that the dissolution of TiO_2 is distinctly dependent on the alkaline medium, being higher in KOH (higher dissolution of Ti(IV)) than in NaOH at the same temperature and equal alkaline concentration [35]. Bavykin et al. experimentally verified that the dissolved Ti(IV) concentration is a key factor that controls the direction of the nanostructure formation [35,36]. They verified that this dissolution effect influenced the route of the precursor transformation and the morphology of the final nanostructures [36]. Further studies should be performed on the solubility of Ecuadorian ilmenite mineral sands to prove if KOH medium in fact promotes a higher dissolution of Ti(IV) than NaOH. Additionally, it should be verified if all the dissolved Ti(IV) can reprecipitate into the desired titanates, but it was beyond the scope of this study.

Summarizing, we have confirmed the feasibility to synthesize 3D hierarchical architectures of well-ordered iron-rich titanate nanosheets from Ecuadorian ilmenite sands through KOH-AHT. Nevertheless, it should be noted that only a partial conversion of the precursor into the desired titanate phase was achieved under the studied conditions. Based on the results of the present work and a number of additional experiments, as mentioned in the Materials and Methods Section, we have found out that the Ecuadorian ilmenite precursor exhibits a high stability in a KOH alkaline medium, since the presence of remaining precursor particles was detected after KOH-AHT at all time spans until 96 h. Thus, in the KOH-AHT products, in addition to the iron-rich titanates, submicron and nanoparticles of IHSSs were also identified.

In this manner, we prepared a material (KOH-AHT product obtained at 72 h) composed of (i) iron-rich titanate nanosheets assembled into 3D hierarchical architectures, and (ii) fine IHSSs (submicron and nanosized), which can be proposed as an inexpensive catalyst candidate. According to the literature, both components show potential applications in this area. For instance, iron-rich layered titanates, as nanosheets, have been employed for the selective catalytic reduction of nitrogen oxide and to degrade organic pollutants, among

others [57,58]. Ilmenite and hematite have also been used as catalysts, within wet peroxide oxidation [59] and heterogeneous electro-Fenton [60].

Additionally, the as-synthesized material has the potential to be used as a filler of polymer composites. Regarding the first component (i), it has been demonstrated that layered titanate fillers (nanotubes and specially nanosheets) have successfully enhanced the mechanical properties of polymer matrices as a counterpart of benchmark graphene-based fillers [28,29]. With respect to the second component (ii), ilmenite- and hematite-based fillers have been employed to improve the barrier properties of polymer matrices against nuclear radiations such as neutrons and gamma rays [61–63]. It is important to highlight that the main advantages of the proposed processing consist of its simplicity, low-cost precursor (USD 24/MT) [17], and, especially, the nanometric size of the as-obtained products.

5. Conclusions

The performance of natural ilmenite sands was assessed as a low-cost precursor in the preparation of nanostructured titanates through one-pot KOH alkaline hydrothermal treatment. The most significant titanate-like products, regarding their morphology, were synthesized after 72 h using a 10 M KOH solution at 180 °C in a sealed reactor. Under these conditions, iron-rich titanate nanosheets assembled as 3D hierarchical architectures were attained. The chemical and phase characterizations suggested that these nanostructures corresponded to highly iron-enriched $K_{2-x}H_xTi_4O_9$ layered titanates. Despite the fact that the complete transformation of the precursor into titanates was not achieved, a potentially promising material was obtained with applications as catalyst, gas sensor, and polymer filler.

Supplementary Materials: The following supporting information can be downloaded at: https://www.mdpi.com/article/10.3390/min13030406/s1: Figure S1: SEM images of KOH-AHTs at 180 °C: (a) KOH (12M)/72 h; (b) KOH (10M)/72 h/~30 bar; (c) KOH (10M)/72 h + 72 h. The squares show remaining precursor particles; Figure S2: Fitting of the Ecuadorian ilmenite sands precursor; Figure S3: SEM images of (a) the surface of the precursor (smooth), and (b) the surface of the remaining precursor after 24 h of KOH-AHT exposure (rougher and flawed areas marked in yellow); Figure S4: Elemental mapping analysis of the KOH-product obtained at 72 h; Figure S5: (a,b) Remaining nanosheets within KOH-product obtained at 96 h.

Author Contributions: K.J.L. designed and performed the experiments supervised by E.P., V.H.G. and P.I.P.; A.D. (Alexis Debut) and K.V. carried out SEM and TEM-SAED analyses; A.D. (Anja Dosen) performed the quantitative XRPD analyses. All authors contributed to the interpretation of the data. K.J.L., B.A.M., E.P., V.H.G. and P.I.P. wrote and edited the paper. All authors have read and agreed to the published version of the manuscript.

Funding: This research received no external funding.

Data Availability Statement: The data presented in this study are available in article or supplementary material.

Acknowledgments: The authors gratefully acknowledge the support from the Escuela Politécnica Nacional (Quito, Ecuador) through the project grant PIM-20-03. The authors are also grateful to M. J. Benitez for the XRPD analyses (Electroceramics Laboratory, Department of Physics, EPN). K.J.L is grateful to C.S. Valdivieso-Ramírez for their technical support. B.A.M. is grateful to CNPq (National Council for Scientific and Technological Development) for a Research Productivity Grant and to FAPERJ (CNE E-26/200.805/2021).

Conflicts of Interest: The authors declare no conflict of interest.

References

1. Zhang, W.; Zhu, Z.; Cheng, C.Y. A literature review of titanium metallurgical processes. *Hydrometallurgy* **2011**, *108*, 177–188. [CrossRef]
2. Kasuga, T.; Hiramatsu, M.; Hoson, A.; Sekino, T.; Niihara, K. Formation of titanium oxide nanotube. *Langmuir* **1998**, *14*, 3160–3163. [CrossRef]

3. Chen, Q.; Zhou, W.; Du, G.H.; Peng, L.-M. Trititanate Nanotubes Made via a Single Alkali Treatment. *Adv. Mater.* **2002**, *14*, 1208–1211. [CrossRef]
4. Bavykin, D.V.; Parmon, V.N.; Lapkin, A.A.; Walsh, F.C. The effect of hydrothermal conditions on the mesoporous structure of TiO_2 nanotubes. *J. Mater. Chem.* **2004**, *14*, 3370–3377. [CrossRef]
5. Morgado, E.; De Abreu, M.A.S.; Pravia, O.R.C.; Marinkovic, B.A.; Jardim, P.M.; Rizzo, F.C.; Araújo, A.S. A study on the structure and thermal stability of titanate nanotubes as a function of sodium content. *Solid State Sci.* **2006**, *8*, 888–900. [CrossRef]
6. Morgan, D.L.; Triani, G.; Blackford, M.G.; Raftery, N.A.; Frost, R.L.; Waclawik, E.R. Alkaline hydrothermal kinetics in titanate nanostructure formation. *J. Mater. Sci.* **2011**, *46*, 548–557. [CrossRef]
7. Kochkar, H.; Lakhdhar, N.; Berhault, G.; Bausach, M.; Abdelhamid, G. Optimization of the alkaline hydrothermal route to titanate nanotubes by a doehlert matrix experience design. *J. Phys. Chem. C* **2009**, *113*, 1672–1679. [CrossRef]
8. Lu, H.; Zhao, J.; Li, L.; Zheng, J.; Zhang, L.; Gong, L.; Wang, Z.; Zhu, Z. A systematic study on evolution mechanism of titanate nanostructures in the hydrothermal process. *Chem. Phys. Lett.* **2011**, *508*, 258–264. [CrossRef]
9. Doong, R.; Kao, I. Fabrication and Characterization of Nanostructured Titanate Materials by the Hydrothermal Treatment Method. *Recent Pat. Nanotechnol.* **2008**, *2*, 84–102. [CrossRef]
10. Simpraditpan, A.; Wirunmongkol, T.; Pavasupree, S.; Pecharapa, W. Simple hydrothermal preparation of nanofibers from a natural ilmenite mineral. *Ceram. Int.* **2013**, *39*, 2497–2502. [CrossRef]
11. Suzuki, Y.; Pavasupree, S.; Yoshikawa, S.; Kawahata, R. Natural rutile-derived titanate nanofibers prepared by direct hydrothermal processing. *J. Mater. Res.* **2005**, *20*, 1063–1070. [CrossRef]
12. Jardim, P.M.; Mancic, L.; Marinkovic, B.A.; Milosevic, O.; Rizzo, F. $Na_{x-y}H_yTi_{2-x}Fe_xO_4 \bullet nH_2O$ nanosheets with lepidocrocite-like layered structure synthesized by hydrothermal treatment of ilmenite sand. *Cent. Eur. J. Chem.* **2011**, *9*, 415–421. [CrossRef]
13. Costa, A.M.L.M.; Marinkovic, B.A.; Suguihiro, N.M.; Smith, D.J.; Da Costa, M.E.H.M.; Paciornik, S. Fe-doped nanostructured titanates synthesized in a single step route. *Mater. Charact.* **2015**, *99*, 150–159. [CrossRef]
14. Mancic, L.T.; Marinkovic, B.A.; Jardim, P.M.; Milosevic, O.B.; Rizzo, F. Precursor Particle Size as the Key Parameter for Isothermal Tuning of Morphology from Nanofibers to Nanotubes in the $Na_{2-x}H_xTi_nO_{2n+1}$ System through Hydrothermal Alkali Treatment of Rutile Mineral Sand. *Cryst. Growth Des.* **2009**, *9*, 2152–2158. [CrossRef]
15. Marinkovic, B.A.; Pontón, P.I.; Resende, J.M.; Letichevsky, S.; Habran, M.; Viol, J.B.; Pandoli, O.; Mancic, L. Lepidocrocite-like ferrititanate nanosheets and their full exfoliation with quaternary ammonium compounds. *Mater. Des.* **2015**, *85*, 197–204. [CrossRef]
16. Marinkovic, B.A.; Mancic, L.; Jardim, P.M.; Milosevic, O.; Rizzo, F. Hydrothermal synthesis of $Na_xFe_xTi_{2-x}O_4$ from natural ilmenite sand: A $CaFe_2O_4$ structure type compound. *Solid State Commun.* **2008**, *145*, 346–350. [CrossRef]
17. Lagos, K.J.; Marinkovic, B.A.; Debut, A.; Vizuete, K.; Guerrero, V.H.; Pardo, E.; Pontón, P.I. Towards iron-titanium oxide nanostructures from ecuadorian black mineral sands. *Minerals* **2021**, *11*, 122. [CrossRef]
18. Wang, A.; Si, Y.; Yin, H.; Chen, J.; Huo, J. Synthesis of Na-, Fe-, and Mg-containing titanate nanocomposites starting from ilmenite and NaOH and adsorption kinetics, isotherms, and thermodynamics of Cu(II), Cd(II), and Pb(II) cations. *Mater. Sci. Eng. B Solid-State Mater. Adv. Technol.* **2019**, *249*, 114411. [CrossRef]
19. Piera, E.; Tejedor-Tejedor, M.I.; Zorn, M.E.; Anderson, M.A. Relationship concerning the nature and concentration of Fe(III) species on the surface of TiO_2 particles and photocatalytic activity of the catalyst. *Appl. Catal. B Environ.* **2003**, *46*, 671–685. [CrossRef]
20. Enhessari, M.; Razi, M.K.; Etemad, L.; Parviz, A.; Sakhaei, M. Structural, optical and magnetic properties of the Fe_2TiO_5 nanopowders. *J. Exp. Nanosci.* **2014**, *9*, 167–176. [CrossRef]
21. Preda, S.; Umek, P.; Zaharescu, M.; Anastasescu, C.; Petrescu, S.V.; Gîfu, C.; Eftemie, D.I.; State, R.; Papa, F.; Balint, I. Iron-Modified Titanate Nanorods for Oxidation of Aqueous Light Irradiation. *Catalysts* **2022**, *12*, 666. [CrossRef]
22. Chezhina, N.V.; Piir, I.V.; Krasnov, A.G.; Koroleva, M.S.; Kellerman, D.G.; Semenov, V.G.; Shalaeva, E.V.; Leonidov, I.I.; Shein, I.R. Structure and Magnetic Properties of a Nanosized Iron-Doped Bismuth Titanate Pyrochlore. *Inorg. Chem.* **2022**, *61*, 13369–13378. [CrossRef] [PubMed]
23. Kaur, A.; Singh, A.; Singh, L.; Mishra, S.K.; Babu, P.D.; Asokan, K.; Kumar, S.; Chen, C.L.; Yang, K.S.; Wei, D.H.; et al. Structural, magnetic and electronic properties of iron doped barium strontium titanate. *RSC Adv.* **2016**, *6*, 112363–112369. [CrossRef]
24. Stenina, I.A.; Sobolev, A.N.; Yaroslavtsev, S.A.; Rusakov, V.S.; Kulova, T.L.; Skundin, A.M.; Yaroslavtsev, A.B. Influence of iron doping on structure and electrochemical properties of $Li_4Ti_5O_{12}$. *Electrochim. Acta* **2016**, *219*, 524–530. [CrossRef]
25. Akieh, M.N.; Lahtinen, M.; Väisänen, A.; Sillanpää, M. Preparation and characterization of sodium iron titanate ion exchanger and its application in heavy metal removal from waste waters. *J. Hazard. Mater.* **2008**, *152*, 640–647. [CrossRef]
26. Fàbrega, C.; Andreu, T.; Cabot, A.; Morante, J.R. Location and catalytic role of iron species in TiO_2: Fe photocatalysts: An EPR study. *J. Photochem. Photobiol. A Chem.* **2010**, *211*, 170–175. [CrossRef]
27. Dosen, A.; Pontón, P.I.; Marinkovic, B.A. Thermally induced phase transformations of lepidocrocite-like ferrititanate nanosheets synthesized from a low cost precursor by hydrothermal method. *Mater. Chem. Phys.* **2017**, *197*, 138–144. [CrossRef]
28. Harito, C.; Bavykin, D.V.; Light, M.E.; Walsh, F.C. Titanate nanotubes and nanosheets as a mechanical reinforcement of water-soluble polyamic acid: Experimental and theoretical studies. *Compos. Part B Eng.* **2017**, *124*, 54–63. [CrossRef]

29. Tamayo-Aguilar, A.; Guaman, M.V.; Guerrero, V.H.; Lagos, K.J.; Costa, C.A.; Nascimento, C.R.; Marinkovic, B.A.; Ponton, P.I. Mechanical properties of amine-cured epoxy composites reinforced with pristine protonated titanate nanotubes. *J. Mater. Res. Technol.* **2020**, *9*, 15771–15778. [CrossRef]
30. Neri, G.; Bonavita, A.; Ipsale, S.; Rizzo, G.; Baratto, C.; Faglia, G.; Sberveglieri, G. Pd- and Ca-doped iron oxide for ethanol vapor sensing. *Mater. Sci. Eng. B* **2007**, *139*, 41–47. [CrossRef]
31. Cao, W.; Tan, O.K.; Pan, J.S.; Zhu, W.; Gopal Reddy, C. V XPS characterization of xα-Fe_2O_3–(1−x)ZrO_2 for oxygen gas sensing application. *Mater. Chem. Phys.* **2002**, *75*, 67–70. [CrossRef]
32. Chen, J.; Xu, L.; Li, W.; Gou, X. α-Fe_2O_3 Nanotubes in Gas Sensor and Lithium-Ion Battery Applications. *Adv. Mater.* **2005**, *17*, 582–586. [CrossRef]
33. Wang, Y.; Wang, S.; Zhao, Y.; Zhu, B.; Kong, F.; Wang, D.; Wu, S.; Huang, W.; Zhang, S. H2S sensing characteristics of Pt-doped α-Fe_2O_3 thick film sensors. *Sensors Actuators B Chem.* **2007**, *125*, 79–84. [CrossRef]
34. Jadhav, V.V.; Patil, S.A.; Shinde, D.V.; Waghmare, S.D.; Zate, M.K.; Mane, R.S.; Han, S.H. Hematite nanostructures: Morphology-mediated liquefied petroleum gas sensors. *Sens. Actuators B Chem.* **2013**, *188*, 669–674. [CrossRef]
35. Bavykin, D.V.; Cressey, B.A.; Light, M.E.; Walsh, F.C. An aqueous, alkaline route to titanate nanotubes under atmospheric pressure conditions. *Nanotechnology* **2008**, *19*, 275604. [CrossRef]
36. Bavykin, D.V.; Cressey, B.A.; Walsh, F.C. Low-temperature synthesis of titanate nanotubes in aqueous KOH. *Aust. J. Chem.* **2007**, *60*, 95–98. [CrossRef]
37. An, Y.; Yin, D.; Song, L.; Chen, Y.; Gao, K. Hydrothermal synthesis and characterisation of titanate nanomaterial thin films in mixed aqueous NaOH/KOH. *Micro Nano Lett.* **2020**, *15*, 313–316. [CrossRef]
38. Lagos, K.J.; Marinkovic, B.A.; Dosen, A.; Guamán, M.V.; Guerrero, V.H.; Pardo, E.; Pontón, P.I. Data on phase and chemical compositions of black sands from "El Ostional" beach situated in Mompiche, Ecuador. *Data Brief* **2020**, *32*, 106214. [CrossRef]
39. Klinger, M. More features, more tools, more CrysTBox. *J. Appl. Crystallogr.* **2017**, *50*, 1226–1234. [CrossRef]
40. Gates-Rector, S.; Blanton, T. The Powder Diffraction File: A quality materials characterization database. *Powder Diffr.* **2019**, *34*, 352–360. [CrossRef]
41. Blesa, M.A.; Morando, P.J.; Regazzoni, A.E. *Chemical Dissolution of Metal Oxides*; CRC Press: Boca Raton, FL, USA, 2018; ISBN 9781315891415.
42. Meng, X.; Wang, Q.; Duan, L.; Chung, J.S. Catalytic combustion of diesel soot over perovskite-type catalyst: Potassium titanates. *Kinet. Catal.* **2012**, *53*, 560–564. [CrossRef]
43. Ide, Y.; Shirae, W.; Takei, T.; Mani, D.; Henzie, J. Merging Cation Exchange and Photocatalytic Charge Separation Efficiency in an Anatase/$K_2Ti_4O_9$ Nanobelt Heterostructure for Metal Ions Fixation. *Inorg. Chem.* **2018**, *57*, 6045–6050. [CrossRef]
44. Saothayanun, T.K.; Sirinakorn, T.T.; Ogawa, M. Ion Exchange of Layered Alkali Titanates ($Na_2Ti_3O_7$, $K_2Ti_4O_9$, and $Cs_2Ti_5O_{11}$) with Alkali Halides by the Solid-State Reactions at Room Temperature. *Inorg. Chem.* **2020**, *59*, 4024–4029. [CrossRef] [PubMed]
45. Lee, S.S.; Byeon, S.H. Structural and morphological behavior of TiO_2 rutile obtained by hydrolysis reaction of $Na_2Ti_3O_7$. *Bull. Korean Chem. Soc.* **2004**, *25*, 1051–1054. [CrossRef]
46. Zainullina, V.M.; Zhukov, V.P.; Denisova, T.A.; Maksimova, L.G. Electronic structure and chemical bonding in monoclinic and cubic $Li_{2-x}H_xTiO_3$ ($0 \leq x \leq 2$). *J. Struct. Chem.* **2003**, *44*, 180–186. [CrossRef]
47. Kukovecz, Á.; Kordás, K.; Kiss, J.; Kónya, Z. Atomic scale characterization and surface chemistry of metal modified titanate nanotubes and nanowires. *Surf. Sci. Rep.* **2016**, *71*, 473–546. [CrossRef]
48. Lu, X.; Liu, F.; Dang, Y.; Li, M.; Ruan, M.; Wu, M.; Zhu, C.; Mani, T.; Suib, S.L.; Gao, P.X. Transition-metal doped titanate nanowire photocatalysts boosted by selective ion-exchange induced defect engineering. *Appl. Surf. Sci.* **2022**, *591*, 153116. [CrossRef]
49. Pang, Y.L.; Lim, S.; Ong, H.C.; Chong, W.T. A critical review on the recent progress of synthesizing techniques and fabrication of TiO_2-based nanotubes photocatalysts. *Appl. Catal. A Gen.* **2014**, *481*, 127–142. [CrossRef]
50. Zhang, Y.; Jiang, Z.; Huang, J.; Lim, L.Y.; Li, W.; Deng, J.; Gong, D.; Tang, Y.; Lai, Y.; Chen, Z. Titanate and titania nanostructured materials for environmental and energy applications: A review. *RSC Adv.* **2015**, *5*, 79479–79510. [CrossRef]
51. Luo, W.; Taleb, A. Large-scale synthesis route of TiO_2 nanomaterials with controlled morphologies using hydrothermal method and TiO_2 aggregates as precursor. *Nanomaterials* **2021**, *11*, 365. [CrossRef]
52. Yang, W.; Chen, H.; Lu, J. Assembly of stacked In_2O_3 nanosheets for detecting trace NO_2 with ultrahigh selectivity and promoted recovery. *Appl. Surf. Sci.* **2021**, *539*, 148217. [CrossRef]
53. Bavykin, D.V.; Walsh, F.C. *Titanate and Titania Nanotubes*; Nanoscience & Nanotechnology Series; Royal Society of Chemistry: Cambridge, UK, 2009; ISBN 978-1-84755-910-4.
54. Wu, D.; Liu, J.; Zhao, X.; Li, A.; Chen, Y.; Ming, N. Sequence of events for the formation of titanate nanotubes, nanofibers, nanowires, and nanobelts. *Chem. Mater.* **2006**, *18*, 547–553. [CrossRef]
55. Xu, L.; Fang, H.; Li, S.; Zhu, J.; Pan, C.; Pan, Y.; Feng, Q. Tailored Hydrothermal Synthesis of Specific Facet-Dominated TiO_2 Nanocrystals from Lepidocrocite-Type Layered Titanate Nanosheets: Systematical Investigation and Enhanced Photocatalytic Performance. *Langmuir* **2020**, *36*, 4477–4495. [CrossRef] [PubMed]
56. Huang, J.; Cao, Y.; Deng, Z.; Tong, H. Formation of titanate nanostructures under different NaOH concentration and their application in wastewater treatment. *J. Solid State Chem.* **2011**, *184*, 712–719. [CrossRef]

57. Chen, X.; Cen, C.; Tang, Z.; Zeng, W.; Chen, D.; Fang, P.; Chen, Z. The key role of ph value in the synthesis of titanate nanotubes-loaded manganese oxides as a superior catalyst for the selective catalytic reduction of NO with NH_3. *J. Nanomater.* **2013**, *2013*, 3. [CrossRef]
58. Kim, T.W.; Ha, H.W.; Paek, M.J.; Hyun, S.H.; Baek, I.H.; Choy, J.H.; Hwang, S.J. Mesoporous iron oxide-layered titanate nanohybrids: Soft-chemical synthesis, characterization, and photocatalyst application. *J. Phys. Chem. C* **2008**, *112*, 14853–14862. [CrossRef]
59. Munoz, M.; Domínguez, P.; de Pedro, Z.M.; Casas, J.A.; Rodriguez, J.J. Naturally-occurring iron minerals as inexpensive catalysts for CWPO. *Appl. Catal. B Environ.* **2017**, *203*, 166–173. [CrossRef]
60. Muzenda, C.; Nkwachukwu, O.V.; Arotiba, O.A. Synthetic Ilmenite ($FeTiO_3$) Nanoparticles as a Heterogeneous Electro-Fenton Catalyst for the Degradation of Tetracycline in Wastewater. *Ind. Eng. Chem. Res.* **2022**, *61*, 11417–11428. [CrossRef]
61. El-Sayed Abdo, A.; El-Sarraf, M.A.; Gaber, F.A. Utilization of ilmenite/epoxy composite for neutrons and gamma rays attenuation. *Ann. Nucl. Energy* **2003**, *30*, 175–187. [CrossRef]
62. Kara, H.; Karabul, Y.; Kılıç, M.; İçelli, O.; Güven Özdemir, Z. Volcanic Rock Reinforced Epoxy Composites for Gamma Ray Shielding. *Eur. J. Sci. Technol.* **2019**, *15*, 552–560. [CrossRef]
63. Eren Belgin, E.; Aycik, G.A.; Kalemtas, A.; Pelit, A.; Dilek, D.A.; Kavak, M.T. Preparation and characterization of a novel ionizing electromagnetic radiation shielding material: Hematite filled polyester based composites. *Radiat. Phys. Chem.* **2015**, *115*, 43–48. [CrossRef]